MATERIALS SCIENCE

Mesoporous amorphous non-noble metals as versatile substrates for high loading and uniform dispersion of Pt-group single atoms

Yunqing Kang[1,2], Shuangjun Li[3], Ovidiu Cretu[4], Koji Kimoto[4], Yingji Zhao[5], Liyang Zhu[5], Xiaoqian Wei[5], Lei Fu[2], Dong Jiang[5], Chao Wan[2], Bo Jiang[3], Toru Asahi[5], Dieqing Zhang[3], Hexing Li[3]*, Yusuke Yamauchi[6,7]*

Atomically dispersed Pt-group metals are promising as nanocatalysts because of their unique geometric structures and ultrahigh atomic utilization. However, loading isolated Pt-group metals in single-atom alloys (SAAs) with distinctive bimetallic sites is challenging. In this study, we present amorphous mesoporous Ni boride (Ni-B) as an ideal substrate to uniformly disperse Pt atoms with tunable loadings (1.7 to 12.2 wt %). The effect of the morphology, composition, and crystal phase of the Ni-B host on the growth and dispersion of Pt atoms is discussed. The resulting amorphous Pt-Ni-B mesoporous nanospheres exhibit superior electrocatalytic H_2 evolution performance in acidic media. This strategy holds the potential to synthesize a diverse library of mesoporous amorphous Pt-group SAAs, by leveraging functional amorphous nanostructured 3*d* transition-metal borides as substrates, thereby proposing a comprehensive strategy to control atomically dispersed Pt-group metals.

INTRODUCTION

Atomically dispersed Pt-group metals have gained attention as a potential material for various catalytic applications because of their ultrahigh metal utilization and unique geometric structure (*1*–*3*). Although the high atomic unsaturated coordination of Pt-group metals affords them high catalytic activity when reduced to the atomic level, such as for forming metal single atoms (SAs), it also makes them prone to instability. One effective approach to address this limitation is combining SAs with specific supports that can modulate the catalytic activity by enhancing the interaction between the metal and support (*4*). Therefore, extensive efforts are currently underway for developing catalysts with a high loading of atomically dispersed noble metals to maximize the utilization of materials that have remarkable catalytic activity but are relatively expensive (*5*, *6*). Thus far, various types of supports, including nitrogen-carbon composites (*7*, *8*), metal oxides (*9*, *10*), and metal sulfides (*11*) have been investigated extensively as ideal substrates for well-dispersed SAs. However, these supports form the oxidation states of the SAs. Another effective approach is forming single-atom alloys (SAAs), where the guest metal is isolated by another metallic substrate (*12*, *13*), thereby enabling the SAAs to exhibit surface metallic states for both the host metal support and the atomically dispersed metal atoms and form bimetallic sites. Consequently, the guest and host metals mutually influence their catalytic performances via metal-metal interactions such as ligand, geometric, and/or lattice strain effects (*14*). The interaction patterns of adsorbed chemical species on individual Pt-group metal atoms within SAAs undergo a change because of the lack of robust interatomic binding locations (*15*), enhancing selectivity and improving resilience against poisoning.

Successful synthesis and effective catalytic performances have been demonstrated for various SAAs of M_1/M_2 (M_1 and M_2 represent an atomically dispersed noble metal and a nonprecious metal substrate, respectively), including Pt/Ni (*16*), Pt/Cu (*17*–*19*), Ir/Co (*20*), and Pd/Cu (*21*). A majority of published SAAs are confined to crystalline NPs without specifically designed nanostructures (*22*). The loading amount of guest SAs in SAA catalysts is restricted, e.g., 0.25, 3.3, and 6.7 wt % for Pt/Ni (*16*), Pt/Co (*23*), and Pt/Cu (*17*), respectively, and increasing the loading content can leads agglomerate and form larger clusters or NPs with segregated phases from the host metal (*17*, *24*). Thus, breaking the inherent crystal lattice constraints of the host metal in SAAs to achieve the uniform dispersion and high loading of guest Pt-group metals remains desired and challenging.

In this study, we show that Ni boride (Ni-B) with an amorphous structure and mesoporous nanospheres (MNs) shape serves as an ideal substrate to achieve the uniform dispersion of atomically dispersed Pt atoms produced through a galvanic replacement reaction (GRR) (table S1). This results in the formation of amorphous Pt-Ni-B (*a*-Pt-Ni-B) SAAs in the MNs form. The loading amount of Pt in *a*-Pt-Ni-B MNs can be controlled easily, reaching as high as 12.2 wt %, without changing the amorphous and mesoporous characteristics of the material. The effects of different morphologies, compositions, and crystal phases (amorphous or crystalline) of Ni-B on the dispersion of Pt atoms and their catalytic properties are explored and highlighted. Further, we use the electrocatalytic hydrogen evolution reaction (HER) as a probe reaction to demonstrate that the prepared *a*-Pt-Ni-B MNs exhibit a low overpotential and high mass activity, making them highly effective catalysts. In addition, our approach displays excellent versatility in synthesizing a wide range of

[1]Nanozyme Laboratory in Zhongyuan, Henan Academy of Innovations in Medical Science, Zhengzhou 451163, Henan, China. [2]Research Center for Materials Nanoarchitectonics, National Institute for Materials Science (NIMS), 1-1 Namiki, Tsukuba, Ibaraki 305-0044, Japan. [3]The Education Ministry Key Lab of Resource Chemistry, Joint International Research Laboratory of Resource Chemistry, Shanghai Frontiers Science Center of Biomimetic Catalysis, College of Chemistry and Materials Science, Shanghai Normal University, Shanghai 200234, China. [4]Electron Microscopy Group, Center for Basic Research on Materials, NIMS, Namiki 1-1, Tsukuba, Ibaraki 305-0044, Japan. [5]Faculty of Science and Engineering, Waseda University, 3-4-1 Okubo, Shinjuku, Tokyo 169-8555, Japan. [6]Australian Institute for Bioengineering and Nanotechnology (AIBN) and School of Chemical Engineering, The University of Queensland, Brisbane, QLD 4072, Australia. [7]Department of Materials Process Engineering, Graduate School of Engineering, Nagoya University, Nagoya 464–8603, Japan.
*Corresponding author. Email: y.yamauchi@uq.edu.au (Y.Y.); hexing-li@shnu.edu.cn (H.L.)

amorphous SAAs MNs with precisely controlled compositions, including *a*-M-Ni-B (M = Pt, Pd, Rh, Ru, and Ir), *a*-Pt-M-Ni-B (M = Rh, Ru, and Ir), and *a*-Pt-Co-B (tables S2 and S3). This study presents a universal approach to control the dispersion and amount of noble SAs and the catalytic properties of the SAAs catalysts by manipulating the phase and morphology of the host metal.

RESULTS

Morphological and structural characterizations

The amorphous Pt-Ni-B MNs (*a*-Pt-Ni-B MNs) were synthesized by a wet chemical reduction with the self-assembly of di-block copolymer micelles, following a GRR. First, bare amorphous Ni-B MNs (*a*-Ni-B MNs) with a well-defined mesoporous morphology of exposed pores and a disordered arrangement of local metal atoms (attributed to the incorporation of B in the Ni lattice) were synthesized based on our previously reported strategy (fig. S1) (*25*). Loading Pt with various contents was achieved through GRR by adding the desired $H_2PtCl_6{\cdot}6H_2O$ aqueous solution to the as-formed mesostructured *a*-Ni-B/micelle suspension (see Materials and Methods for details). A typical sample with a Pt mass loading of 9.1 wt % [determined by inductively coupled plasma–optical emission spectroscopy (ICP-OES); table S1] on *a*-Ni-B MNs is denoted as *a*-$Pt_{9.1}$-Ni-B MNs.

Scanning electron microscopy (SEM) images showed a well-defined mesoporous structure for *a*-$Pt_{9.1}$-Ni-B MNs, and the exposed pores were observed outside the nanospheres (Fig. 1A and B). The average sizes of the nanospheres and the pores were ~118 and ~11 nm (fig. S2), respectively, as illustrated in Fig. 1C. The porous morphology of *a*-$Pt_{9.1}$-Ni-B MNs was observed using transmission electron microscopy (TEM) and high-angle annular dark-field scanning TEM (HAADF-STEM) images. Figure 1 (D and E) shows that abundant mesopores extend from the exterior to the interior of the spherical structure, enabling the reactants to diffuse deeply. Mesopores offer not only a substantial increase in the active surface area but also the presence of rough surfaces, creating highly favorable conditions for efficiently distributing active sites and facilitating adsorption, diffusion, and desorption of reactants, intermediates, and products. Selected-area electron diffraction (SAED) pattern shown in the inset of Fig. 1D indicates that one *a*-$Pt_{9.1}$-Ni-B MN is amorphous without a long-range order. The *a*-$Pt_{9.1}$-Ni-B MNs have a core-shell structure where the Pt atoms are distributed on the outer surface and the Ni atoms are dominant in the core (Fig. 1F and G). Electron energy-loss spectroscopy (EELS) analyses identify the existence and uniform distribution of B atoms throughout *a*-$Pt_{9.1}$-Ni-B MNs (fig. S3).

The well-defined mesoporous structure of *a*-$Pt_{9.1}$-Ni-B MNs was confirmed using small-angle x-ray scattering (SAXS) and the N_2 adsorption-desorption isotherm. As shown in fig. S4A, a single peak located at $q = 0.32$ nm^{-1} indicates the periodicity of mesopores in *a*-$Pt_{9.1}$-Ni-B MNs. The pore-to-pore distance is calculated as ~19.6 nm. The N_2 adsorption-desorption isotherm (fig. S4B) indicates the mesoporous structure of *a*-$Pt_{9.1}$-Ni-B MNs, which have a Brunauer-Emmett-Teller (BET) surface area of ~32.5 m^2 g^{-1}.

Powder x-ray diffraction (XRD) profiles of *a*-$Pt_{9.1}$-Ni-B MNs show a broad peak without any diffraction peaks of face center cubic (fcc) Pt, indicating the amorphous alloying of Pt and Ni-B (Fig. 2A). As shown in Fig. 2B, no well-resolved lattice fringes are observed in the high-resolution HAADF-STEM images, thereby verifying the amorphous structure without a discernible long-range order in *a*-$Pt_{9.1}$-Ni-B MNs, which is consistent with the XRD observations. The rich atomically dispersed Pt atoms can be distinguished from the edge region of the mesoporous walls (Fig. 2B and fig. S5), wherein some possible Pt atoms are circled in red (Fig. 2C). In contrast, the phase structure of the *a*-$Pt_{9.1}$-Ni-B MNs was converted to the crystalline phase in the reference crystalline $Pt_{9.1}$-Ni-B (denoted as *c*-$Pt_{9.1}$-Ni-B) MNs prepared via annealing (400°C) *a*-$Pt_{9.1}$-Ni-B under Ar atmosphere for 2 hours (fig. S6). The *c*-$Pt_{9.1}$-Ni-B exhibits a single-phase alloy structure without phase segregation even after increasing the annealing temperature to 900°C (fig. S7), confirming

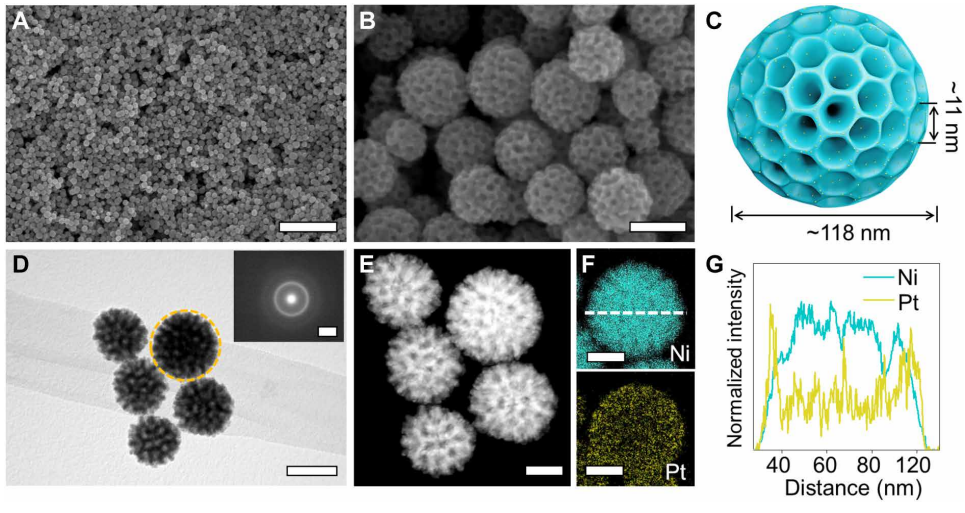

Fig. 1. Structural characterization of core-shell *a*-$Pt_{9.1}$-Ni-B MNs. (**A**) Low-magnification scanning electron microscopy (SEM; scale bar, 1 μm), (**B**) high-magnification SEM (scale bar, 100 nm), (**C**) illustration of a single MN, (**D**) transmission electron microscopy (TEM) image (scale bar, 100 nm), (**E**) high-angle annular dark-field scanning TEM images (HAADF-STEM; scale bar, 50 nm), (**F**) elemental energy-dispersive x-ray spectroscopy (EDS) maps (scale bar, 100 nm), and (**G**) corresponding normalized line-scan profiles of *a*-$Pt_{9.1}$-Ni-B sample. The inset of (D) shows the SAED pattern from a single MN (scale bar, 5 nm^{-1}).

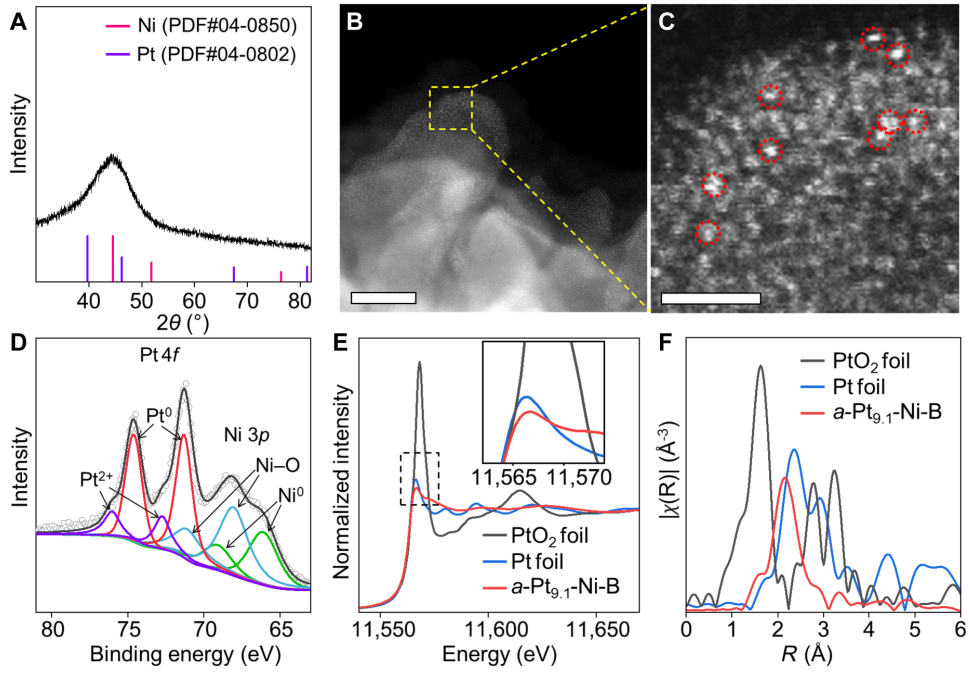

Fig. 2. Structural and surface characterizations of *a*-$Pt_{9.1}$-Ni-B MNs. (**A**) Powder x-ray diffraction (XRD) pattern. (**B**) High-resolution HAADF-STEM image (scale bar, 5 nm). (**C**) Enlarged HAADF-STEM image (scale bar, 1 nm) of the selected area of (B). The bright spots (circled in red) represent the possible positions of atomically dispersed Pt atoms. (**D**) XPS spectra of Pt 4*f* and Ni 3*p*. Pt L_{III}-edge (**E**) x-ray absorption near the edge structure and (**F**) Fourier transform extended x-ray absorption fine structure of *a*-$Pt_{9.1}$-Ni-B MNs with standard references (shoulder peaks located between 1.5 and 2.0 Å of both Pt foil and *a*-$Pt_{9.1}$-Ni-B originate from the slight surface oxidation of Pt during the ex situ XAS measurement process).

that Pt atoms are highly dispersed into the lattice of the host Ni-B. These data indicate that the bonding between heterometals, that is, Pt-Ni in our case, is stronger than that of homometallic bonding (i.e., Pt-Pt), which ensures no bonding between Pt atoms.

X-ray photoelectron spectroscopy (XPS) and x-ray absorption spectra (XAS) were used to investigate the electronic state and local coordination environment of Pt and Ni atoms of *a*-$Pt_{9.1}$-Ni-B MNs. The Pt $4f_{7/2}$ and $4f_{5/2}$ main peaks of *a*-$Pt_{9.1}$-Ni-B are loaded at 71.3 and 74.6 eV, respectively, which confirm its dominant nature as metallic Pt (Fig. 2D). The peaks located at 72.7 and 76.1 eV indicate the coexistence of Pt^{2+}. Both metallic and oxidized states of Ni are observed (Fig. 2D and fig. S8A). Owing to the strong attraction for O, B atoms exist in an oxidized state on the surface (i.e., B-O) (fig. S8B). Compared to the homemade Pt nanoparticles (NPs), the peaks belonging to Pt 4*f* in *a*-$Pt_{9.1}$-Ni-B MNs shift negatively (fig. S9), confirming the effect of Ni-B on the electronic structure of Pt. XAS offers an additional understanding of the characteristics of the Pt and Ni species of *a*-$Pt_{9.1}$-Ni-B MNs. As shown in Fig. 2E, the Pt L_{III}-edge x-ray absorption near edge structure (XANES) data confirm that the valence state of Pt is close to the standard Pt foil with a weaker intensity of the white line, suggesting the negatively charged nature of Pt in *a*-$Pt_{9.1}$-Ni-B MNs. The slightly electron-enriched Pt species was reported to be favorable for HER (*26*). The Ni K-edge, which is located between Ni foil and NiO, provides evidence for the partial oxidation of Ni in *a*-$Pt_{9.1}$-Ni-B (fig. S10A). These observations align well with the findings from the XPS results. The formation of atomically dispersed Pt atoms on *a*-Ni–B MNs is confirmed by the absence of a Pt-Pt scattering path in the Fourier transforms extended x-ray absorption fine spectra (EXAFS) of Pt L_{III}-edge (Fig. 2F). One prominent peak (at ~2.16 Å) positioned between the Pt foil and standard PtO_2 sample indicates the formation of the Pt-Ni alloy, aligning with the reported EXAFS data showing the presence of isolated Pt atoms on Cu (*17*) or Ru (*27*) NPs. The presence of single Pt atom on the *a*-Ni-B MNs is supported by the fitting results, as shown in fig. S11 and table S4. The data reveal that *a*-$Pt_{9.1}$-Ni-B MNs show a Pt-Ni coordination number (CN) of ~7.33 at 2.57 Å, which is different from the Pt-Pt CN of 12 at 2.77 Å in the Pt foil. In addition, the absence of detectable Pt-Pt, Pt-O, and Pt-B coordination contributions in *a*-$Pt_{9.1}$-Ni-B MNs suggests that Pt atoms are predominantly distributed as isolated entities, surrounded by Ni atoms, as evidenced by the wavelet transform (WT) contour plot (fig. S12). The amorphous nature of Ni-B is retained after the formation of the Pt-Ni SAA, as confirmed by absence of the long-range order in the EXAFS curve (fig. S10B) and the corresponding fitting data with the lower CN and shorter Ni-Ni distance compared to that of the Ni foil (table S4). The XAS results validate the existence of the Pt-Ni SAAs, characterized by the presence of atomically dispersed Pt atoms on *a*-Ni-B MNs.

GRR process study

Achieving a uniform atomic-level dispersion of Pt atoms on Ni nanostructures is challenging because a GRR occurs rapidly during the synthesis process when metallic Ni nanostructures mix with Pt salts. The rapid GRR and large Ni-Pt lattice mismatch leads to the random atomic mixing of Ni and Pt, as well as a loss of control over the nanostructure (*28*–*30*). Our approach achieves the atomic-level dispersion of Pt effortlessly without the need to stringently control GRR conditions by adjusting the coordination environment of Ni,

i.e., by forming short-range ordered and long-range disordered amorphous structures. Figure 3A shows an illustration of the synthesis route of *a*-Pt-Ni-B MNs using the proposed strategy. Initially, mesostructured Ni-B/micelles composites were obtained using polystyrene-poly(ethylene oxide) (PS-*b*-PEO) block copolymer micelles as the pore-directing agent. Pt atoms were then inserted into the parent Ni-B sacrificial template by GRR, forming the highly well distribution of Pt atoms, as shown in the SEM–energy-dispersive x-ray spectroscopy (SEM-EDS) results for the *a*-$Pt_{9.1}$-Ni-B MNs (fig. S13). Owing to the gap of standard reduction potentials (E_0) between the Ni^{2+}/Ni and $[PtCl_6]^{2-}$/Pt pairs (the E_0 of Ni^{2+}/Ni, $[PtCl_6]^{2-}$/$[PtCl_4]^{2-}$, and $[PtCl_4]^{2-}$/Pt is −0.26, 0.73, 0.76 V versus standard hydrogen electrode, SHE, respectively) (table S2) (*31*–*33*). Pt ions are rapidly reduced to metallic Pt atoms when contacted with metallic Ni atoms of *a*-Ni-B, thereby causing metallic Ni atoms to be oxidized to Ni^{2+} as

$$[PtCl_6]^{2-}{}_{(aq)} + 2Ni_{(s)} \rightarrow Pt_{(s)} + 2Ni^{2+}{}_{(aq)} + 6Cl^{-}{}_{(aq)} \quad (1)$$

Pt atoms preferentially replace the outer Ni atoms because of the first contact with Ni on the surface of MNs; however, some Pt atoms probably penetrate deeper into the *a*-Ni-B MNs because of the presence of abundant interconnected channels within the mesoporous shape. The preferential replacement of the surface metallic Ni atoms of *a*-Ni-B MNs results in the final core-shell structure of *a*-$Pt_{9.1}$-Ni-B with a Pt-rich shell, as identified from the above HAADF-STEM data (Figs. 1, G and H, and 2B; and fig. S5).

Further, we investigated the effect of the synthesis conditions, including reaction time, temperature, and concentration/type of Pt precursor of GRR on the final morphology and disordered structure of *a*-Pt-Ni-B MNs. Changes in the content of Ni and Pt elements in different GRR time demonstrate that the occurrence of the GRR between $[PtCl_6]^{2-}$ ions and metallic Ni atoms (Fig. 3B). For the synthesis of *a*-$Pt_{9.1}$-Ni-B MNs, the content of Pt in MNs increases gradually with an increase in GRR time, whereas the Ni content decreases gradually, retaining the similar mesoporous morphology, as determined by the SEM and SEM-EDS results (Fig. 3B and fig. S14). The reaction temperature plays an important role in redox reactions. Predictably, the GRR rate between Ni and Pt atoms increases with an increase in the GRR temperature. Therefore, increased reaction temperatures (i.e., 40°, 60°, and 70°C) were applied to explore the effect of the reaction rate on the Pt dispersion and structure. As shown in fig. S15, the mesoporous morphology, well-distribution of Pt, and amorphous natures do not change with an increase in the GRR temperature. Unlike the sample prepared using GRR, the co-reduction of the Ni^{2+} and $[PtCl_6]^{2-}$ precursors with dimethylamine borane (DMAB) as a reducing agent leads to a formation of aggregated NPs and separated phases (fig. S16).

In amorphous transition-metal borides, the wide range of adjustable compositions between the metal and B offers promising opportunities for adjusting the morphology, phase structure, electronic properties, adsorption performance, etc. of the catalysts (*34*–*36*). Therefore, in addition to various GRR preparation parameters, the effect of the content of B in the host *a*-Ni-B MNs on the final morphology of *a*-Pt-Ni-B was also evaluated. During the preparation process of *a*-Ni-B MNs, DMAB is used as both a primary reducing agent and a B source (*36*). The content of B in Ni-B can be adjusted

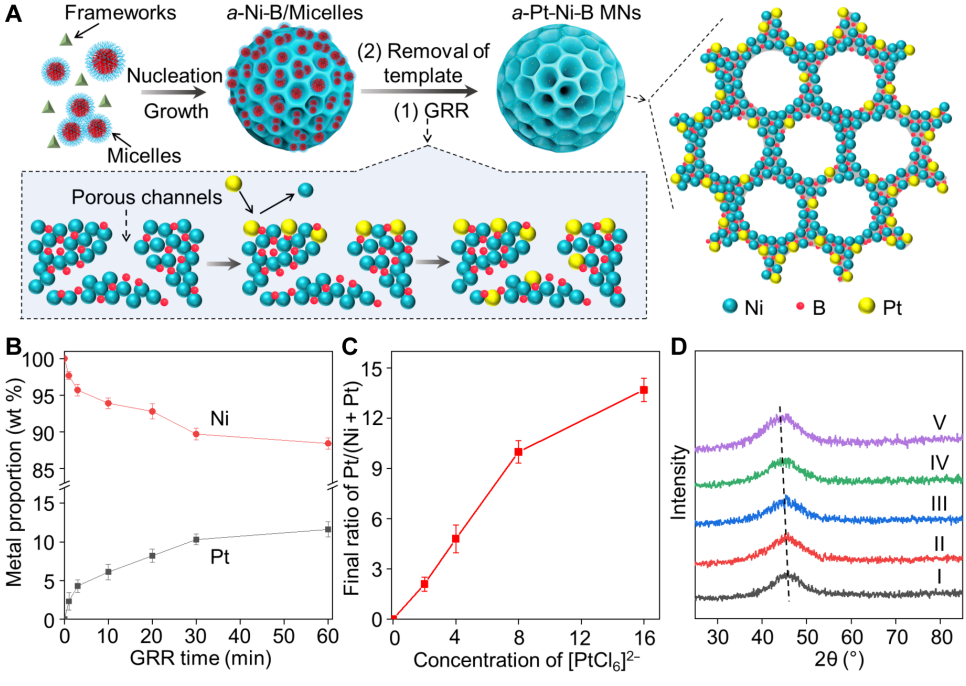

Fig. 3. Synthesis of *a*-Pt-Ni-B MNs through GRR. (**A**) Illustration of the synthesis route, including the micelle-induced wet chemical reduction synthesis of mesostructured *a*-Ni-B/micelles and the following loading of Pt through GRR. (**B**) Evolution content of Ni and Pt in the *a*-Pt-Ni-B MNs during GRR at different reaction times. (**C**) Relationship between the concentrations of Pt precursor (i.e., $[PtCl_6]^{2-}$) and final mass ratios of Pt/(Pt + Ni). (**D**) XRD patterns of *a*-Pt-Ni-B MNs with different loading contents of Pt: (I) *a*-Ni–B, (II) *a*-$Pt_{1.7}$-Ni-B, (III) *a*-$Pt_{3.9}$-Ni-B, (IV) *a*-$Pt_{9.1}$-Ni-B, and (V) *a*-$Pt_{12.2}$-Ni-B MNs. Error bars in (B) and (C) that correspond to the SD of three independent measurements.

by changing the concentration of DMAB, which does not affect the amorphous nature of the obtained samples (fig. S17A). Although there is no obvious aggregation of Pt NPs when the DMAB concentration decreases from 1.0 to 0.125 M, the surface of the MNs is wrapped by a flocculent layer at low DMAB concentrations (i.e., 0.125 and 0.25 M). At high DMAB concentrations (i.e., 0.5 and 1.0 M), the surface of the MNs is kept clean (fig. S17, B to E). These results indicate that a higher concentration of DMAB can result in more metal-metalloid (i.e., Ni-B) bonds with more metallic Ni on the surface, thereby ensuring sufficient Ni atoms to be replaced by Pt in the GRR. In this study, 0.5 M DMAB was used to prepare *a*-Ni-B unless stated otherwise.

The loading content of Pt is controlled easily by varying the concentrations of $H_2PtCl_6{\cdot}6H_2O$ (1.0 ml of 2.0, 4.0, 8.0, and 16.0 mM aqueous $H_2PtCl_6{\cdot}6H_2O$). Four *a*-Pt-Ni-B samples with increased Pt mass loadings of 1.7, 3.9, 9.1 and 12.2 wt % are denoted as *a*-Pt_x-Ni-B, where *x* displays the weight percent of the Pt loading (Fig. 3C), as determined by ICP-OES (table S1). The mesoporous structure remains as the increased Pt loading ratio (fig. S18). Further, with more Pt replaced by Ni, the broad peak of XRD gradually shifts toward the lower angle, demonstrating the successfully incorporated Pt with a larger lattice within the disordered matrix of Ni-B (Fig. 3D). The proportion of guest metal (M_1) to host metal (M_2) in SAAs is low to ensure that M_1 atoms do not bind with each other (*5*). Although crystal M_2 may contain some structural defects, such as segregation and dislocations, the strong metallic bonding (M_2-M_2) interactions in the host metal M_2 makes it challenging to accommodate a large loading of isolated guest M_1. Thus, the loading of M_1 in most SAAs is usually less than 8 wt % (*22*). However, in our material, the Pt/(Pt + Ni) ratio in *a*-$Pt_{9.1}$-Ni-B MNs can easily reach 9.7 wt % (even 13.0 wt % in *a*-$Pt_{12.2}$-Ni-B MNs) (Fig. 3C), which is considerably higher than that commonly observed in other SAAs. The aberration correction HAADF-STEM image confirms isolated Pt atoms on the Ni-B of *a*-$Pt_{12.2}$-Ni-B MNs (fig. S19); however, further increasing the loading amount of Pt results in the appearance of some microcrystalline Pt, as confirmed by HAADF-STEM images and the XRD pattern (fig. S20). We can reasonably assume that the metallic amorphous state of M_2 with local disordered atomic arrangement possesses the ability to break away from the lattice constraints observed in conventional crystalline metals, thereby achieving a substantial loading of atomically dispersed M_1.

Reference hosts were prepared using crystalline Ni-B, crystalline Ni, and nonporous amorphous Ni-B as sacrificial matrices for loading Pt to explore the effect of mesoporous morphology and long-range disordered arrangement of atoms of Ni-B on the GRR process. Amorphous alloys are temperature-sensitive materials susceptible to transitions to the crystalline state at high-temperature treatments. Therefore, the crystalline mesoporous Ni-B (*c*-Ni-B) sample was synthesized via the thermal treatment of the prepared *a*-Ni-B for 2 hours at 400°C under Ar atmosphere. Further, the crystalline Ni nanothorn (*c*-Ni) without doping B was synthesized by replacing DMAB with hydrazine hydrate. Then, the Pt atoms were deposited on the surface of the as-generated *c*-Ni-B and *c*-Ni through GRR, thereby resulting in the Pt-*c*-Ni-B (fig. S21) and Pt-*c*-Ni (fig. S22), respectively. Compared to *a*-$Pt_{9.1}$-Ni-B, the distribution of Pt atoms on both *c*-Ni-B and *c*-Ni are more random, and part of the aggregated Pt NPs were observed (figs. S21, B to D, and S22D). The XRD patterns in figs. S21E and S22C confirm the crystalline structure of Pt-*c*-Ni-B and Pt-*c*-Ni with separated fcc Ni (PDF#04-0850) and fcc Pt (PDF#04-0802) phases. A nonporous Ni-B nanosphere matrix was synthesized when preparing *a*-Ni-B while omitting PS-*b*-PEO (fig. S23, A and B). Although an amorphous structure is still formed, similar to *a*-$Pt_{9.1}$-Ni-B MNs, after loading Pt on nonporous Ni-B nanospheres (np-Pt-Ni-B) (fig. S23C), the Pt atoms are randomly distributed around on the surface of the nonporous Ni-B, probably because of the lower surface area and considerably smoother surface of the nonporous Ni-B nanospheres compared to that of *a*-Ni-B MNs (fig. S23D). These results suggest that atomically distributed Pt atoms on *a*-$Pt_{9.1}$-Ni-B MNs originated from the disordered arrangement of Ni atoms of *a*-Ni-B. Compared to the crystalline phase, the amorphous state has a large number of unsaturated coordination sites and hanging bonds, as well as a uniform distributed structure defects (*37*), which facilitates the dispersion of guest Pt atoms. In addition, the bumpy surface of Ni-B MNs with abundant atomic steps and kinks ensures a more homogeneous dispersion of Pt around the mesopores (Fig. 4A), thereby verifying the contribution of the porous structure to the distribution of the guest metal atoms in the GRR.

Library synthesis

Our strategy can be extended to synthesize various other noble–non-noble metal borides, such as *a*-M-Ni-B (M = Pt/Rh/Ir/Ru/Pd/Au) MNs (Fig. 4, B to E, and figs. S24 to S30), with precise compositional and experimental control. Despite the diverse reduction potentials of these noble metals, the standard reduction potentials of M^{x+}/M pairs of noble metals are more positive than that of the Ni^{2+}/Ni pair (table S2), which is the driving force for the GRR. However, the potentials listed here represent the value in the standard state only. The actual value of the reduction potential may be also affected by pH, concentrations of relevant ions, coordination environment, and other nonstandard conditions (*38*). For example, the higher standard reduction potential (E_0, 1.0 V versus SHE) for the $[AuCl_4]^-$/Au pair is more positive than that of the $[PtCl_6]^{2-}/[PtCl_4]^{2-}$ (0.73 V versus SHE) and $[PtCl_4]^{2-}$/Pt (0.76 V versus SHE) pairs, resulting in crystalline-amorphous Au-Ni-B nanocomposites with crystalline Au on the shell and amorphous Ni-B core (fig. S24). This result is consistent with our previous work on the Au-CoFeB composite (*39*). However, although the E_0 of Ir^{3+}/Ir (1.16 V versus SHE) is higher than that of the $[AuCl_4]^-$/Au pair, amorphous Ir-Ni-B (i.e., *a*-$Ir_{6.0}$-Ni-B) MNs are produced without observing the crystalline state of Ir (Fig. 4C). Furthermore, when an aqueous Na_2PdCl_4 precursor was used for GRR, the crystalline Pd presented on the surface of the Ni-B MNs despite a lower reduction potential (0.59 V versus SHE for $[PdCl_4]^{2-}$/Pd) than that of the Pt-based pair (fig. S25). Further, amorphous Pd-Ni-B (i.e., *a*-$Pd_{7.8}$-Ni-B) MNs were synthesized when $Pd(acac)_2$ dissolved in acetone was used instead of that dissolved in aqueous Na_2PdCl_4 (Fig. 4E). These results demonstrate that the driving force of GRR does not simply depend on the E_0 gap between guest metal and parent substrate; the crystal phase and morphology of the host, precursor of the guest metal, and reaction conditions also need to be considered. Thus, besides *a*-Pt-Ni-B MNs, a library synthesis of four other core-shell amorphous mesoporous M_x-Ni-B (i.e., *a*-M_x-Ni-B, M = Rh, Ir, Ru, Pd; *x* represents the corresponding mass loadings; table S3) alloys were performed using a similar strategy. Figure 4 (B to E) shows the SEM, HAADF-STEM, and corresponding EDS elemental mappings, as well as the high-resolution TEM (HRTEM) images of *a*-$Rh_{2.0}$-Ni-B, *a*-$Ir_{6.0}$-Ni-B, *a*-$Ru_{3.1}$-Ni-B, and *a*-$Pd_{7.8}$-Ni-B MNs, respectively. The

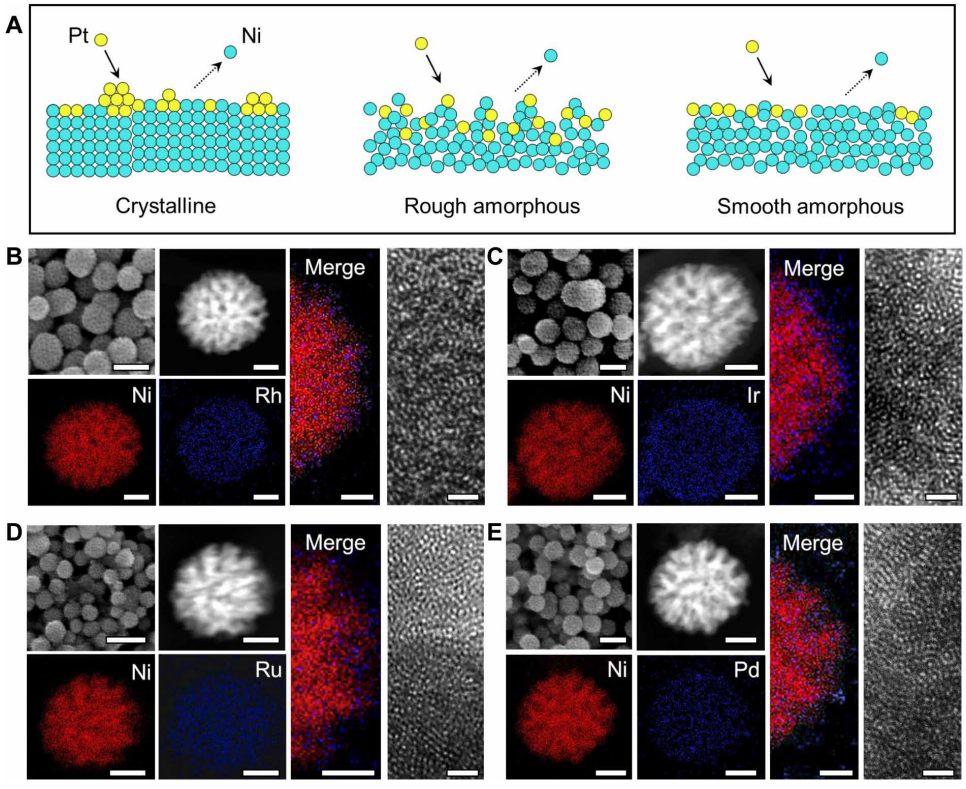

Fig. 4. Library synthesis of *a*-M-Ni-B MNs. (**A**) Schematic of the effect of host structure on the dispersion of guest metals. SEM (scale bars, 100 nm), HAADF-STEM and EDS maps (scale bars, 40 nm), merge of Ni (red) and M (blue) (scale bar, 20 nm), HRTEM images (scale bars, 1 nm) of *a*-M-Ni-B MNs: (**B**) *a*-$Rh_{2.0}$-Ni-B, (**C**) *a*-$Ir_{6.0}$-Ni-B, (**D**) *a*-$Ru_{3.1}$-Ni-B, and (**E**) *a*-$Pd_{7.8}$-Ni-B.

well-defined mesoporous shapes of *a*-$Rh_{2.0}$-Ni-B, *a*-$Ir_{6.0}$-Ni-B, *a*-$Ru_{3.1}$-Ni-B, and *a*-$Pd_{7.8}$-Ni-B MNs are confirmed by the SEM and HAADF-STEM results. The corresponding EDS maps demonstrate the core-shell structure with a Ni-B–dominant core and the noble metal–rich shell in all *a*-M_x-Ni-B MNs. The HRTEM images and the XRD patterns suggest the amorphous natures of all *a*-M_x-Ni-B MNs (Fig. 4, B to E, and fig. S26).

The composition of noble metals on *a*-Ni-B MNs is not limited to a single noble metal element but can include two noble metals elements, as exemplified by *a*-Pt-Ru-Ni-B, *a*-Pt-Ir-Ni-B, and *a*-Pt-Rh-Ni-B (figs. S27 to S29). Further, the mesoporous host can be substituted with other amorphous 3*d* transition-metal borides, such as *a*-Co-B MNs, thereby forming *a*-Pt-Co-B (fig. S30). With appropriate control over the preparation conditions, the composition of both the host mesoporous amorphous non-noble metal borides and guest noble metals can be considerably adjusted. Therefore, this approach offers notable command over both the composition and mesoscopic structure/morphology of disordered noble–non-noble metal borides, making it possible to discover interesting new disordered alloys and tailor the performance in their midst.

Electrocatalytic HER performance

Electrocatalytic water splitting, driven by renewable electricity, offers a green path for producing highly pure hydrogen through the cathode HER, thereby providing a promising approach to realize a carbon-neutral energy society (*40*, *41*). Mainstream electrolysis systems for water splitting include alkaline water electrolysis and acidic water electrolysis (*42*). Compared to the alkaline environment, acidic water electrolysis has advantages of high partial load range and high current density; however, the corrosive acidic environments require the utilization of costly Pt-based noble catalysts, which increases the overall stack cost (*43*). The preparation of atomic-dispersed Pt catalysts not only improves the atomic utilization of Pt to reduce cost but also exhibits excellent HER reactivity (*44*, *45*).

In this study, we evaluated the HER performance of the prepared *a*-Pt-Ni-B catalysts in an Ar-saturated 0.5 M H_2SO_4 solution using a three-electrode system. The commercial carbon-supported Pt (Pt/C) containing 20 wt % Pt was used as the reference catalysts for comparison. The linear sweep voltammetry (LSV) measurements unveils that Pt atoms are the active center for the acidic HER, and the optimal catalyst is *a*-$Pt_{9.1}$-Ni-B MNs (Fig. 5A and fig. S31). When normalized on a geometrical surface area, *a*-$Pt_{9.1}$-Ni-B requires an overpotential of 11 mV to reach a current density of 10 mA cm^{-2}, which is greater than the 18 mV of the Pt/C catalyst (Fig. 5B). The mass activity, normalized by the loading amount of Pt, of *a*-$Pt_{9.1}$-Ni-B at an overpotential of 50 mV is 30.0 A mg_{Pt}^{-1} (20.7 times higher than that of the commercial Pt/C), which indicates the high intrinsic catalytic of *a*-$Pt_{9.1}$-Ni-B. Such a low overpotential and high mass activity over *a*-$Pt_{9.1}$-Ni-B still have high levels relative to other reported atomically dispersed Pt-based electrocatalysts in acidic media (Fig. 5C and table S5) (*44*, *46*–*61*). Cyclic voltammetry (CV) studies reveal that our *a*-$Pt_{9.1}$-Ni-B catalyst exhibits a different hydrogen adsorption/desorption curve in comparison to Pt/C (fig. S32) because of the low loading amount of Pt on the electrode. The

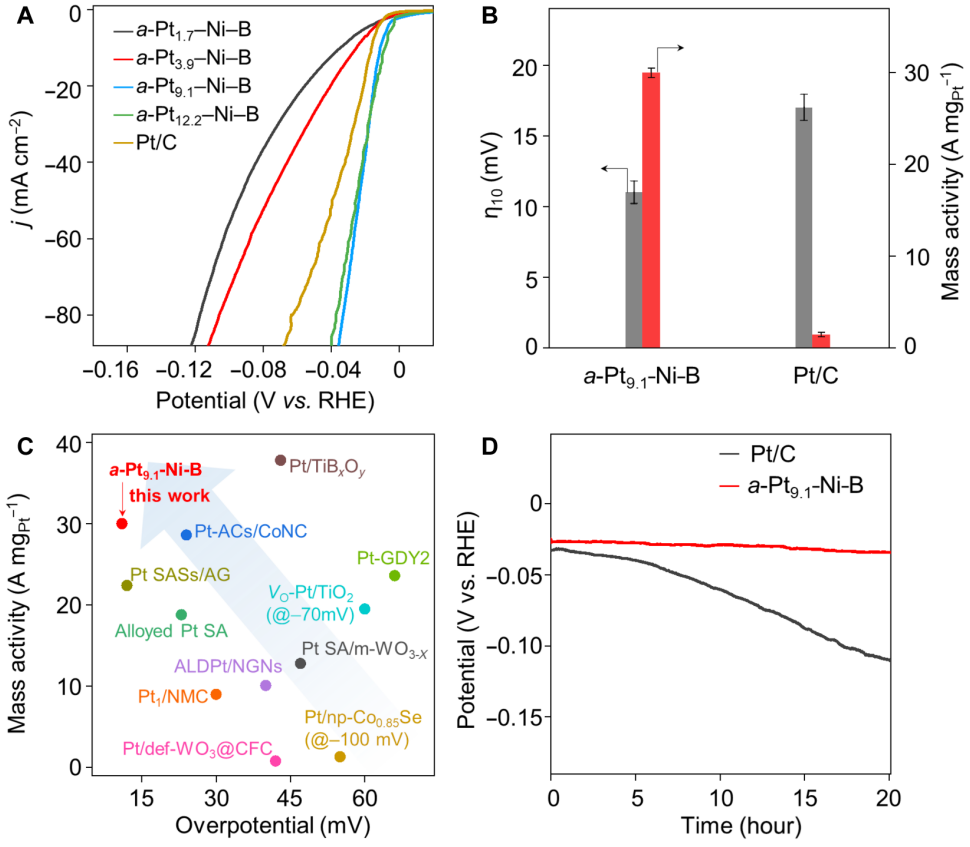

Fig. 5. Electrochemical HER performance in acidic media. (**A**) Polarization curves after the manual *iR* correction of *a*-Pt-Ni-B MNs with various Pt contents and commercial Pt/C in the 0.5 M H_2SO_4 electrolyte at a scan rate of 2 mV s^{-1}. (**B**) Comparison of overpotentials (@10 mA cm^{-2}) and mass activities normalized by Pt loading on the electrode at −50 mV for *a*-$Pt_{9.1}$-Ni-B MNs and Pt/C. Error bars correspond to the SD based on three independent measurements. (**C**) Comparison of overpotentials at 10 mA cm^{-2} and mass activities at overpotential of 50 mV with *a*-$Pt_{9.1}$-Ni-B that reported Pt-based HER catalysts in acidic electrolytes. (**D**) CP recorded on *a*-$Pt_{9.1}$-Ni-B MNs and Pt/C at a constant current density of 10 mA cm^{-2}.

enhanced HER kinetics of *a*-$Pt_{9.1}$-Ni-B are verified through Nyquist plots and Tafel analyses. The Nyquist plots show that *a*-$Pt_{9.1}$-Ni-B had a smaller semicircular diameter in the electrochemical impedance spectra compared to that of Pt/C, suggesting the lower charge transfer resistance and faster HER kinetics of *a*-$Pt_{9.1}$-Ni-B (fig. S33A) (*62*). In addition, *a*-$Pt_{9.1}$-Ni-B has a lower Tafel slope of 27 mV dec^{-1} compared to that of the Pt/C catalyst (29 mV dec^{-1}) (fig. S33B). The values of the Tafel slopes suggest that the well-accepted Volmer-Tafel mechanism with the Tafel-step (i.e., hydrogen desorption) limited pathway in the acidic environment occurred on both *a*-$Pt_{9.1}$-Ni-B and Pt/C (*63*). The experimental measurements of H_2 production closely align with the theoretical values, indicating a high Faradaic efficiency (FE) of ~100% (fig. S34) for *a*-$Pt_{9.1}$-Ni-B. Further, the higher HER activity of *a*-$Pt_{9.1}$-Ni-B than that of np-Pt-Ni-B, *c*-$Pt_{9.1}$-Ni-B, and Pt-*c*-Ni catalysts verifies its structural and compositional advantages (fig. S35).

The comparatively high catalytic stability of *a*-$Pt_{9.1}$-Ni-B MNs for the acidic HER was confirmed by chronopotentiometry (CP) and CV cycles tests. Our CP studies reveal that the overpotential increased by only 9 mV over the *a*-$Pt_{9.1}$-Ni-B catalyst in a 20-hour continuous test. For comparison, Pt/C catalyst exhibits a 78-mV overpotential increase under the same conditions (Fig. 5D). In addition, after 200 and 2000 CV cycling tests, the *a*-$Pt_{9.1}$-Ni-B catalyst exhibits superior preservation of its original catalytic activity compared to that with the Pt/C catalyst (fig. S36). We characterized the *a*-$Pt_{9.1}$-Ni-B catalyst using TEM, SAED, HAADF-STEM, and XPS measurements to investigate the structural transformation of the catalyst after CV stability testing (figs. S37 to S39). The results show that, after the 200 CV cycling test, the *a*-$Pt_{9.1}$-Ni-B catalyst largely maintained its initial mesoporous morphology and amorphous structure (fig. S37). The EDS maps and corresponding line-scan profiles confirm the out-shell predominantly distributed Pt, while some microcrystallines are observed on the edge site, probably because of the aggregation of Pt atoms after leaching metallic Ni under acidic condition measurements (fig. S38). However, the surface of the catalyst remains composed of metallic Pt, as confirmed by the XPS results (fig. S39). In contrast, the decline in the HER activity of Pt/C catalyst can be attributed to the evident particle agglomeration and growth after the CV stability test, possibly resulting from aggregation and/or Ostwald ripening (fig. S40).

We conducted density functional theory (DFT) calculations to analyze the *d*-band center shift and hydrogen adsorption free energy (ΔG_{H^*}) on the Pt and Pt-Ni-B model (fig. S41, A and B) to gain deeper insights into the origin of the high HER catalytic performance of *a*-$Pt_{9.1}$-Ni-B MNs. The density of states of the topmost Pt atomic layer of the Pt and Pt-Ni-B surfaces are shown in fig. S41C. The

d-band center of Pt-Ni-B is −2.23 eV, which was downshifted in comparison to that of bare Pt (−2.16 eV). According to the *d*-band center theory (*64*), the lower *d*-band center indicates a weaker interaction binding between the active sites and surface hydrogen adsorption. Therefore, the modulating ΔG_{H^*} is determined to be −0.2 eV on Pt-Ni-B, which is closer to zero compared to the value of −0.26 eV observed on Pt (fig. S41D). In HER, a lower value of $|\Delta G_{H^*}|$ (i.e., closer to zero) indicates enhanced adsorption and desorption capabilities, leading to excellent HER performance (*65*). Moreover, the Bader charge analysis confirms the electron-enriched Pt sites on Pt-Ni-B, indicating that the modulated electronic structure of Pt (fig. S42) is consistent with the XPS and XANES results. Therefore, the above theoretical results can potentially clarify why our synthesized material, *a*-$Pt_{9.1}$-Ni-B, demonstrates superior electrochemical HER activity compared to that of pure Pt in the experiments.

DISCUSSION

We showed that fabricating amorphous and mesoporous structures of Ni-B can help achieve atomically dispersed Pt atoms, thereby forming SAAs. Both local long-range disordered atomic arrangement Ni atoms and rich structural steps/kinks of Ni-B ensure the uniform dispersion and easily controllable loading content of Pt (ranging from 1.7 to 12.2 wt %). The prepared *a*-Pt-Ni-B samples have isolated Pt atoms, amorphous phases, bimetallic surface states, and well-defined mesoporous shape. Owing to the high density of Pt active sites and metal-metal interactions in SAAs, typical *a*-$Pt_{9.1}$-Ni-B MNs exhibit a modified electronic structure and reduced hydrogen binding energy, as confirmed from experimental and DFT calculation results. In acidic HER, the *a*-$Pt_{9.1}$-Ni-B catalyst demonstrates a low overpotential (11 mV@10 mA cm^{-2}) and high mass activity (30.0 A mg_{Pt}^{-1}@−50 mV), thereby surpassing commercial Pt/C and most single Pt-based catalysts. This synthetic method can be extended to other mesoporous amorphous noble–non-noble metal borides with atomically dispersed noble metals, such as *a*-M-Ni-B (M = Pt, Pd, Rh, Ru, and Ir), *a*-Pt-M-Ni-B (M = Rh, Ru, and Ir), and *a*-Pt-Co-B. Our results indicate that when preparing SAAs using GRR, besides considering the redox potential gap between the host and guest metals, the loading amount and dispersion of the guest metal depend greatly on the phase and morphology of the host.

MATERIALS AND METHODS

Chemicals

All reagents were used as purchased without further purification. Nickel(II) acetate tetrahydrate [$Ni(OAc)_2{\cdot}4H_2O$], cobalt(II) acetate tetrahydrate [$Co(OAc)_2{\cdot}4H_2O$], iron (III) chloride hexahydrate ($FeCl_3{\cdot}6H_2O$), chloroplatinic acid hexahydrate ($H_2PtCl_6{\cdot}6H_2O$), palladium(II) acetylacetonate [$Pd(acac)_2$], sodium hexachlororhodate(III) (Na_3RhCl_6), ruthenium(III) chloride ($RuCl_3$), iridium(III) chloride hydrate ($IrCl_3{\cdot}xH_2O$), tetrabutylphosphonium bromide (Bu_4PBr), sodium borohydride (SBH), DMAB, Pluronic F-127 (F127), hydrazine hydrate (N_2H_4, 50 to 60%), and Nafion perfluorinated resin solution (5 wt % in a mixture of lower aliphatic alcohols and water; containing 45% water) were purchased from Sigma-Aldrich. The block copolymer poly(styrene)$_{5000}$-*b*-poly(ethylene oxide)$_{2000}$ (PS-*b*-PEO) (average molecular weight of the corresponding blocks is shown in subscript numbers) was obtained from Polymer Source. *N*,*N*-dimethylformamide (DMF) and acetone were purchased from Nacalai Tesque Inc.

Synthesis of *a*-Ni-B MNs

The *a*-Ni-B MNs were synthesized by a wet chemical reduction with an assembly of the diblock copolymer micelles method (*25*). In brief, 10-mg PS-*b*-PEO was completely dissolved in 3.0 ml of DMF in a double-neck flask to form a uniform solution under sonication. Then, 3.0 ml of H_2O, 4.0 ml of aqueous 60 mM $Ni(OAc)_2{\cdot}4H_2O$ (containing 0.3-g Bu_4PBr), and 6.0 ml of aqueous 0.5 M DMAB solution were added in the above solution. The mixed solution in the flask was purged with Ar and kept in an oil bath at 40°C under gentle stirring for 5.0 min. Next, 30 μl of freshly prepared SBH aqueous solution (1.0 mg/ml) was injected into the flask to initiate the reduction process. The solution gradually developed bubbles and transitioned from light green to black. Subsequently, it reacted for 1.0 hour, resulting in the *a*-Ni-B/micelle suspension. Nonporous amorphous Ni-B nanospheres were synthesized similar to *a*-Ni-B MNs by omitting the block copolymer.

Synthesis of *a*-Pt-Ni-B MNs

The *a*-Pt-Ni-B MNs were synthesized by a GRR. The prepared *a*-Ni-B/micelle suspension was cooled to room temperature (~22°C), and then 1.0 ml of the desired concentration of $H_2PtCl_6{\cdot}6H_2O$ (i.e., 2.0, 4.0, 8.0, and 16 mM) aqueous solution was added dropwise with stirring and kept for 1.0 hour to prepare *a*-Pt_x-Ni-B (*x* displayed the weight percent of Pt loading) MNs. Last, the product was collected by centrifugation and washed several times with acetone/ethanol. For comparison, np-Pt-Ni-B nanospheres were synthesized similar to *a*-Pt-Ni-B MNs without using the block copolymer.

Synthesis of *c*-Pt-Ni-B MNs

The reference *c*-$Pt_{9.1}$-Ni-B MNs sample was prepared by thermally treating the pristine typical amorphous *a*-$Pt_{9.1}$-Ni-B MNs at 400°C in Ar atmosphere for 2.0 hours.

Synthesis of Pt-*c*-Ni-B composites

The *c*-Ni-B sample was prepared by thermally treating the dried *a*-Ni-B MNs powder at 400°C in Ar atmosphere for 2.0 hours. The obtained black powder was redispersed on 10 ml of acetone, followed by adding 1.0 ml of 8.0 mM $H_2PtCl_6{\cdot}6H_2O$ aqueous solution (Ar prepurged) dropwise. After 1.0 hour of reaction, the final Pt-*c*-Ni-B composites were collected by centrifugation and washed several times with acetone.

Synthesis of Pt-*c*-Ni composites

The Pt-*c*-Ni composites were prepared as another comparison sample. To this end, 100 mg of F127 was dissolved in 3.0 ml of H_2O under sonication, followed by adding 3.0 ml of H_2O, 4.0 ml of 60 mM $Ni(OAc)_2{\cdot}4H_2O$, and 6.0 ml of N_2H_4, in sequence. After purging with Ar for 5.0 min, the reaction solution was heated to 80°C in an oil bath and vigorous stirred for 4.0 hours. Then, the produced suspension was cooled down to 22°C and 1.0 ml of 8.0 mM $H_2PtCl_6{\cdot}6H_2O$ aqueous solution (Ar prepurged) was added in dropwise manner. After 1.0 hour of reaction, the final product was collected by centrifugation and washed several times with acetone/ethanol.

Synthesis of *a*-M-Ni-B (M = Rh, Ir, Ru, and Pd) MNs

The *a*-M-Ni-B (M = Rh, Ir, Ru, and Pd) MNs were prepared similar to *a*-Pt-Ni-B MNs; however, the noble metal precursors (temperature for GRR) were changed to 1.0 ml of aqueous 8.0 mM Na_3RhCl_6 (22°C), aqueous 8.0 mM $IrCl_3{\cdot}xH_2O$ (22°C), aqueous 8.0 mM $RuCl_3$ (22°C), and 8.0 mM $Pd(acac)_2$ (0°C) (dissolving in acetone) to synthesize *a*-$Rh_{2.0}$-Ni-B, *a*-$Ir_{6.0}$-Ni-B, *a*-$Ru_{3.1}$-Ni-B, and *a*-$Pd_{7.8}$-Ni-B, respectively.

Synthesis of *a*-Pt-M-Ni-B (M = Ru, Rh, and Ir) MNs

The *a*-Pt-M-Ni-B MNs were prepared similar to *a*-Pt-Ni-B MNs; however, the metal precursor of $H_2PtCl_6{\cdot}6H_2O$ (8.0 mM, 1.0 ml) was changed to $H_2PtCl_6{\cdot}6H_2O$ (8.0 mM, 0.8 ml), followed by adding $RuCl_3$ (8.0 mM, 0.2 ml), Na_3RhCl_6 (8.0 mM, 0.2 ml), and $IrCl_3{\cdot}xH_2O$ (8.0 mM, 0.2 ml) for *a*-Pt-Ru-Ni-B, *a*-Pt-Rh-Ni-B, and *a*-Pt-Ir-Ni-B MNs, respectively.

Synthesis of *a*-Pt-Co-B MNs

The *a*-Pt-Co-B MNs were prepared in the same manner as *a*-Pt-Ni-B; however, the *a*-Co-B/micelle suspension was used instead of the *a*-Ni-B/micelle suspension. The *a*-Co-B/micelle suspension was prepared similar to the *a*-Ni-B/micelle suspension, wherein $Co(OAc)_2{\cdot}4H_2O$ was used instead of $Ni(OAc)_2{\cdot}4H_2O$ according to the published method (*25*).

Characterizations

An ICP-OES was performed on Agilent 5800 to determine the compositions of M-Ni-B (M = Pt, Rh, Ir, Ru, and Pd) MNs. The morphologies of the samples were characterized using a field-emission SEM (Hitachi SU-8000, 10 kV) and a TEM (JEOL JEM-2100F; accelerating voltage, 200 kV). SEM-EDS was observed using a flat quad EDS (5060F, Bruker). The beam spot size for TEM-EDX mapping was set to 0.5 nm. HAADF-STEM images were obtained using a Thermo Fisher Scientific Titan microscope with an acceleration voltage of 300 kV and a probe current of ~30 pA. The EELS spectra and spectrum images were collected using a Gatan Continuum spectrometer. The XPS spectra were obtained on a PHI Quantera SXM (ULVAC-PHI) under an excitation source of focused monochromatic Al Kα x-ray. The energies for all high-resolution spectra were calibrated using the C 1*s* main peak as 284.8 eV. The samples for XPS were fabricated in a glove box after drying in vacuum to avoid surface oxidation. Powder XRD measurements were collected with a Smart lab x-ray diffractometer (RIGAKU) with a step size of 2° min^{-1} using a Cu Kα radiation (40 kV, 30 mA) source. The diffraction peaks corresponding to the pore-to-pore distance were obtained by the XRD pattern in a small angle region using SAXS measurements (Rigaku NANO-Viewer). N_2 adsorption-desorption isotherms were acquired from a BELSORP-mini (BEL, Japan) at 77 K and the pore size distributions were calculated based on the Barrett-Joyner-Halenda model.

XAS measurements and data processing

Ex situ XAS measurements used to characterize the *a*-$Pt_{9.1}$-Ni-B MNs at the Ni K-edge and Pt L_{III}-edge were performed at the BL14W1 station in the Shanghai Synchrotron Radiation Facility (SSRF) (Shanghai, China). The electron storage ring of SSRF was operated at 3.5 GeV with a maximum current of 200 mA. The XAS data were collected using a fixed-exit Si (111) double-crystal monochromator. A Lytle detector was used to collect the fluorescence signal, and the energy was calibrated using a metal foil. The obtained XAS data were processed in the ATHENA module of the IFEFFIT software package. The EXAFS contributions were separated from different coordination shells using a Hanning windows (dk = 1.0 $Å^{-1}$). Subsequently, quantitative curve fittings were performed in the *R*-space (1.0 to 3.0 Å) with a Fourier transform *k*-space range of (3 to 12.5 $Å^{-1}$) using the module ARTEMIS of IFEFFIT. During the curve fitting, the overall amplitude reduction factor S_0^2 was fixed to the best-fit values of 0.83 and 0.80 determined from fitting the data of the metal Pt foil and Ni foil, respectively. Structural parameters such as the CN, interatomic distance (*R*), Debye-Waller factor (σ^2), and edge-energy shift (ΔE_0) were allowed to vary during the fitting process. For the WT analysis, the $\chi(k)$ exported from ATHENA was imported into the Hama Fortran code. The parameters were *R* range = 0 to 6 Å, *k* range = 0 to 14 $Å^{-1}$, and *k* weight = 2. The Morlet function with $\kappa = 10$ and $\sigma = 1$ was used as the mother wavelet to provide the overall distribution.

Electrochemical measurements

Electrochemical measurements (using CHI 660EZ) were conducted using a three-electrode system with graphite rod and Ag/AgCl (saturated KCl) as the counter and reference electrodes, respectively. The reference electrode was calibrated with respect to the reversible hydrogen electrode (RHE) using a high-purity hydrogen saturated three-electrode system (i.e., $E_{RHE} = E_{Ag/AgCl} + 0.23$). The working electrode was prepared by dropping the ink solution onto a rotating disk electrode (RDE; 0.0706 cm^2). The ink solution was prepared by dispersing the as-prepared Pt-Ni-B–based samples (1.0 mg) and Vulcan XC-72 carbon (4.0 mg) in a solution of 980 μl of ethanol and 20 μl of Nafion under sonication, and 3.2 μl of the ink was dropped onto the RDE. The catalyst was first activated by CV scanning for 200 cycles, and then LSV was conducted at a scan rate of 2 mV s^{-1} in an Ar-saturated electrolyte (0.5 M H_2SO_4, pH = 0.2) stirred at 1600 rpm without ohmic drop correction. Tafel plots were derived from the overpotential at different range versus the log (current density) according to the corresponding LSV curves ($\eta = a + b \log |j|$, where η, *a*, *b*, and *j* represent the overpotential, exchange current density, Tafel slope, and current density, respectively). Electrochemical impedance spectroscopy was measured at the different potentials with a frequency range from 10^5 to 0.01 Hz. The resistance of the solution (R_s) resulting from the Nyquist plot was used to correct the ohmic drop (*iR*-correction) for the HER measurement. The corrected potential could be obtained by $E_{corrected} = E_{RHE} - iR_s$. Electrocatalytic durability tests were conducted by subjecting the ink catalyst loaded on carbon fiber paper (with a loading of 1.0 mg cm^{-2}) to CP measurements. Before CP measurements, the catalyst underwent 200 CV cycles at a scan rate of 50 mV s^{-1} to establish stable catalytic performance. Gas products generated at the cathode side were collected in a gas-tight H-type cell to determine the FE of the catalyst. The gas product (i.e., H_2) was confirmed using gas chromatography (Shimadzu Tracera, BID-2010), and the experimental amount of H_2 was measured using a drainage method. Then, the FE was calculated by comparing the experimental H_2 production with the theoretically calculated value.

Computational details

The calculations were performed in the framework of the DFT with the projector augmented plane-wave method, as implemented in the Vienna ab initio simulation package (*66*). The generalized

gradient approximation proposed by Perdew-Burke-Ernzerhof was selected for the exchange correlation potential (*67*). The long-range van der Waals interaction was described by the DFT-D3 approach (*68*). The Pt-Ni-B system was constructed based on a $2 \times 2 \times 2$ of the primitive cell of the fcc phase where five Pt atoms were substituted by three Ni atoms, and two additional B atoms were added to the octahedral sites. The number of atoms of the model was set based on the compositions of stabilized Pt-Ni-B catalyst after HER, determined by ICP-OES. The Pt-Ni-B structure was fully relaxed until the residual forces on the atoms declined to less than 0.02 eV/Å. The cut-off energy for the plane wave was set to 450 eV. The energy criterion was set to 10^{-5} eV in the iterative solution of the Kohn-Sham equation. Brillouin zone integration was performed using a $10 \times 10 \times 10$ *k*-mesh. The Pt-Ni-B (111) surface was constructed based on 2×2 of its primitive cells, containing eight atomic layers (10 Pt, six Ni, and four B atoms). The Pt (111) surface was constructed based on 2×2 of its primitive cells, containing four atomic layers (16 Pt atoms). A vacuum layer of 15 Å was added perpendicular to the slabs to avoid artificial interaction between periodic images. For the Pt-Ni-B surface, the upper three layers were allowed to relax, whereas the bottom five layers were fixed. For Pt (111) surface, the upper two layers were allowed to relax, whereas the bottom two layers were fixed. For calculating the surfaces, the symmetry was removed, and Brillouin zone integration was performed using a $6 \times 6 \times 1$ k-mesh, thereby leading to 36 *k*-points for *k*-points sampling. Further, the dipole correlation was considered for the surface calculations.

The ΔG_{H^*} (change in the Gibbs free energy before and after hydrogen adsorption) was used as an indicator for evaluating the performance of HER. $\Delta G_{H^*} = G_{surface+H} - G_{surface} + G_{H2}/2$, $G_{surface+H}$ was the Gibbs free energy of the surface with hydrogen adsorption, $G_{surface}$ was the Gibbs free energy of the surface, and G_{H2} was the Gibbs free energy of the hydrogen gas. The value of $|\Delta G_{H^*}|$ closer to zero suggested better HER performance. The hydrogen adsorption Gibbs free energy under standard atmospheric pressure was defined as $G_{surface+H} = E_{surface+H} + \Delta G(T)$, where $E_{surface+H}$ was the total energy of the surface with hydrogen adsorption calculated by the DFT; $\Delta G(T) = \Delta E_{ZPE} + \Delta H(T) - \Delta S(T)$, where ΔE_{ZPE}, $\Delta H(T)$, and $\Delta S(T)$ denote the contributions of the zero-point energy, enthalpy, and entropy to the Gibbs free energy attributed to hydrogen adsorption, respectively. $G_{surface}$ was approximated as $E_{surface}$ because the correction of the $\Delta G(T)$ to the Gibbs free energy of the surface could be cancelled out before and after hydrogen adsorption. The calculation of $\Delta G(T)$ was performed by the VASPKIT Package (*69*), and T was used as 298.2 K.

Supplementary Materials

This PDF file includes:

Figs. S1 to S42

Tables S1 to S5

REFERENCES AND NOTES

1. Y. Chen, J. Lin, B. Jia, X. Wang, S. Jiang, T. Ma, Isolating single and few atoms for enhanced catalysis. *Adv. Mater.* **34**, e2201796 (2022).
2. Y. Yao, S. Hu, W. Chen, Z.-Q. Huang, W. Wei, T. Yao, R. Liu, K. Zang, X. Wang, G. Wu, W. Yuan, T. Yuan, B. Zhu, W. Liu, Z. Li, D. He, Z. Xue, Y. Wang, X. Zheng, J. Dong, C.-R. Chang, Y. Chen, X. Hong, J. Luo, S. Wei, W.-X. Li, P. Strasser, Y. Wu, Y. Li, Engineering the electronic structure of single atom Ru sites *via* compressive strain boosts acidic water oxidation electrocatalysis. *Nat. Catal.* **2**, 304–313 (2019).
3. H. Zhou, Y. Zhao, J. Gan, J. Xu, Y. Wang, H. Lv, S. Fang, Z. Wang, Z. Deng, X. Wang, P. Liu, W. Guo, B. Mao, H. Wang, T. Yao, X. Hong, S. Wei, X. Duan, J. Luo, Y. Wu, Cation-exchange induced precise regulation of single copper site triggers room-temperature oxidation of benzene. *J. Am. Chem. Soc.* **142**, 12643–12650 (2020).
4. R. Lang, X. Du, Y. Huang, X. Jiang, Q. Zhang, Y. Guo, K. Liu, B. Qiao, A. Wang, T. Zhang, Single-atom catalysts based on the metal-oxide interaction. *Chem. Rev.* **120**, 11986–12043 (2020).
5. A. Wang, J. Li, T. Zhang, Heterogeneous single-atom catalysis. *Nat. Rev. Chem.* **2**, 65–81 (2018).
6. S. K. Kaiser, Z. Chen, D. Faust Akl, S. Mitchell, J. Pérez-Ramírez, Single-atom catalysts across the periodic table. *Chem. Rev.* **120**, 11703–11809 (2020).
7. L. Han, H. Cheng, W. Liu, H. Li, P. Ou, R. Lin, H.-T. Wang, C.-W. Pao, A. R. Head, C.-H. Wang, X. Tong, C.-J. Sun, W.-F. Pong, J. Luo, J.-C. Zheng, H. L. Xin, A single-atom library for guided monometallic and concentration-complex multimetallic designs. *Nat. Energy* **21**, 681–688 (2022).
8. P. Kuang, Y. Wang, B. Zhu, F. Xia, C.-W. Tung, J. Wu, H. M. Chen, J. Yu, Pt single atoms supported on N-doped mesoporous hollow carbon spheres with enhanced electrocatalytic H_2-evolution activity. *Adv. Mater.* **33**, e2008599 (2021).
9. V. Muravev, A. Parastaev, Y. van den Bosch, B. Ligt, N. Claes, S. Bals, N. Kosinov, E. J. M. Hensen, Size of cerium dioxide support nanocrystals dictates reactivity of highly dispersed palladium catalysts. *Science* **380**, 1174–1179 (2023).
10. D. Jiang, G. Wan, J. Halldin Stenlid, C. E. García-Vargas, J. Zhang, C. Sun, J. Li, F. Abild-Pedersen, C. J. Tassone, Y. Wang, Dynamic and reversible transformations of subnanometre-sized palladium on ceria for efficient methane removal. *Nat. Catal.* **6**, 618–627 (2023).
11. Z. Shi, X. Zhang, X. Lin, G. Liu, C. Ling, S. Xi, B. Chen, Y. Ge, C. Tan, Z. Lai, Z. Huang, X. Ruan, L. Zhai, L. Li, Z. Li, X. Wang, G.-H. Nam, J. Liu, Q. He, Z. Guan, J. Wang, C.-S. Lee, A. R. J. Kucernak, H. Zhang, Phase-dependent growth of Pt on MoS_2 for highly efficient H_2 evolution. *Nature* **621**, 300–305 (2023).
12. R. T. Hannagan, G. Giannakakis, M. Flytzani-Stephanopoulos, E. C. H. Sykes, Single-atom alloy catalysis. *Chem. Rev.* **120**, 12044–12088 (2020).
13. G. Kyriakou, M. B. Boucher, A. D. Jewell, E. A. Lewis, T. J. Lawton, A. E. Baber, H. L. Tierney, M. Flytzani-Stephanopoulos, E. C. H. Sykes, Isolated metal atom geometries as a strategy for selective heterogeneous hydrogenations. *Science* **335**, 1209–1212 (2012).
14. F. Tao, Y. Li, A new type of catalysts: Catalysts of singly dispersed bimetallic sites. *Trends Chem.* **5**, 486–499 (2023).
15. C. J. Wrasman, A. Boubnov, A. R. Riscoe, A. S. Hoffman, S. R. Bare, M. Cargnello, Synthesis of colloidal Pd/Au dilute alloy nanocrystals and their potential for selective catalytic oxidations. *J. Am. Chem. Soc.* **140**, 12930–12939 (2018).
16. S. Kim, J. Lauterbach, E. Sasmaz, Yolk–shell Pt-NiCe@SiO_2 single-atom-alloy catalysts for low-temperature dry reforming of methane. *ACS Catal.* **11**, 8247–8260 (2021).
17. X. Zhang, G. Cui, H. Feng, L. Chen, H. Wang, B. Wang, X. Zhang, L. Zheng, S. Hong, M. Wei, Platinum–copper single atom alloy catalysts with high performance towards glycerol hydrogenolysis. *Nat. Commun.* **10**, 5812 (2019).
18. G. Sun, Z.-J. Zhao, R. Mu, S. Zha, L. Li, S. Chen, K. Zang, J. Luo, Z. Li, S. C. Purdy, A. J. Kropf, J. T. Miller, L. Zeng, J. Gong, Breaking the scaling relationship *via* thermally stable Pt/Cu single atom alloys for catalytic dehydrogenation. *Nat. Commun.* **9**, 4454 (2018).
19. M. D. Marcinkowski, M. T. Darby, J. Liu, J. M. Wimble, F. R. Lucci, S. Lee, A. Michaelides, M. Flytzani-Stephanopoulos, M. Stamatakis, E. C. H. Sykes, Pt/Cu single-atom alloys as coke-resistant catalysts for efficient C–H activation. *Nat. Catal.* **10**, 325–332 (2018).
20. J. Kang, Q.-Y. Fan, W. Zhou, Q. Zhang, S. He, L. Yue, Y. Tang, L. Nguyen, X. Yu, Y. You, H. Chang, X. Liu, L. Chen, Y. Liu, F. Tao, J. Cheng, Y. Wang, Iridium boosts the selectivity and stability of cobalt catalysts for syngas to liquid fuels. *Chem* **8**, 1050–1066 (2022).
21. M. Chhetri, M. Wan, Z. Jin, J. Yeager, C. Sandor, C. Rapp, H. Wang, S. Lee, C. J. Bodenschatz, M. J. Zachman, F. Che, M. Yang, Dual-site catalysts featuring platinum-group-metal atoms on copper shapes boost hydrocarbon formations in electrocatalytic CO_2 reduction. *Nat. Commun.* **14**, 3075 (2023).
22. T. Shen, S. Wang, T. Zhao, Y. Hu, D. Wang, Recent advances of single-atom-alloy for energy electrocatalysis. *Adv. Energy Mater.* **12**, 2201823 (2022).
23. X. Cheng, Y. Wang, Y. Lu, L. Zheng, S. Sun, H. Li, G. Chen, J. Zhang, Single-atom alloy with Pt-Co dual sites as an efficient electrocatalyst for oxygen reduction reaction. *Appl Catal B* **306**, 121112 (2022).
24. Y. Peng, Z. Geng, S. Zhao, L. Wang, H. Li, X. Wang, X. Zheng, J. Zhu, Z. Li, R. Si, J. Zeng, Pt single atoms embedded in the surface of Ni nanocrystals as highly active catalysts for selective hydrogenation of nitro compounds. *Nano Lett.* **18**, 3785–3791 (2018).
25. Y. Kang, B. Jiang, J. Yang, Z. Wan, J. Na, Q. Li, H. Li, J. Henzie, Y. Sakka, Y. Yamauchi, T. Asahi, Amorphous alloy architectures in pore walls: Mesoporous amorphous NiCoB alloy spheres with controlled compositions via a chemical reduction. *ACS Nano* **14**, 17224–17232 (2020).
26. H. Tan, B. Tang, Y. Lu, Q. Ji, L. Lv, H. Duan, N. Li, Y. Wang, S. Feng, Z. Li, C. Wang, F. Hu, Z. Sun, W. Yan, Engineering a local acid-like environment in alkaline medium for efficient hydrogen evolution reaction. *Nat. Commun.* **13**, 2024 (2022).

27. A. R. Poerwoprajitno, L. Gloag, J. Watt, S. Cheong, X. Tan, H. Lei, H. A. Tahini, A. Henson, B. Subhash, N. M. Bedford, B. K. Miller, P. B. O'Mara, T. M. Benedetti, D. L. Huber, W. Zhang, S. C. Smith, J. J. Gooding, W. Schuhmann, R. D. Tilley, A single-Pt-atom-on-Ru-nanoparticle electrocatalyst for CO-resilient methanol oxidation. *Nat. Catal.* **5**, 231–237 (2022).
28. G. Ercolano, F. Farina, L. Stievano, D. J. Jones, J. Rozière, S. Cavaliere, Preparation of Ni@Pt core@shell conformal nanofibre oxygen reduction electrocatalysts via microwave-assisted galvanic displacement. *Cat. Sci. Technol.* **9**, 6920–6928 (2019).
29. C. Li, X. Chen, L. Zhang, S. Yan, A. Sharma, B. Zhao, A. Kumbhar, G. Zhou, J. Fang, Synthesis of core@shell Cu-Ni@Pt-Cu nano-octahedra and their improved MOR activity. *Angew. Chem. Int. Ed.* **60**, 7675–7680 (2021).
30. Y. Chen, Z. Liang, F. Yang, Y. Liu, S. Chen, Ni–Pt core–shell nanoparticles as oxygen reduction electrocatalysts: Effect of Pt shell coverage. *J. Phys. Chem. C* **115**, 24073–24079 (2011).
31. B. Jiang, C. Li, V. Malgras, Y. Yamauchi, Synthesis of ternary PtPdCu spheres with three-dimensional nanoporous architectures toward superior electrocatalysts. *J. Mater. Chem. A* **3**, 18053–18058 (2015).
32. Y. Kang, J. Henzie, H. Gu, J. Na, A. Fatehmulla, B. S. A. Shamsan, A. M. Aldhafiri, W. A. Farooq, Y. Bando, T. Asahi, B. Jiang, H. Li, Y. Yamauchi, Mesoporous metal–metalloid amorphous alloys: The first synthesis of open 3D mesoporous Ni-B amorphous alloy spheres via a dual chemical reduction method. *Small* **16**, e1906707 (2020).
33. B. Jiang, H. Ataee-Esfahani, C. Li, S. M. Alshehri, T. Ahamad, J. Henzie, Y. Yamauchi, Mesoporous trimetallic PtPdRu spheres as superior electrocatalysts. *Chem. A Eur. J.* **22**, 7174–7178 (2016).
34. H. Li, H. Li, W. Dai, M. Qiao, Preparation of the Ni-B amorphous alloys with variable boron content and its correlation to the hydrogenation activity. *Appl. Catal. A. Gen.* **238**, 119–130 (2003).
35. J. Wu, M. Hou, Z. Chen, W. Hao, X. Pan, H. Yang, W. Cen, Y. Liu, H. Huang, P. W. Menezes, Z. Kang, Composition engineering of amorphous nickel boride nanoarchitectures enabling highly efficient electrosynthesis of hydrogen peroxide. *Adv. Mater.* **34**, e2202995 (2022).
36. Y. Kang, Y. Tang, L. Zhu, B. Jiang, X. Xu, O. Guselnikova, H. Li, T. Asahi, Y. Yamauchi, Porous nanoarchitectures of nonprecious metal borides: From controlled synthesis to heterogeneous catalyst applications. *ACS Catal.* **12**, 14773–14793 (2022).
37. B. Jiang, H. Xue, P. Wang, H. Du, Y. Kang, J. Zhao, S. Wang, W. Zhou, Z. Bian, H. Li, J. Henzie, Y. Yamauchi, Noble-metal–metalloid alloy architectures: Mesoporous amorphous iridium–tellurium alloy for electrochemical N_2 reduction. *J. Am. Chem. Soc.* **145**, 6079–6086 (2023).
38. X. Xia, Y. Wang, A. Ruditskiy, Y. Xia, 25th anniversary article: Galvanic replacement: A simple and versatile route to hollow nanostructures with tunable and well-controlled properties. *Adv. Mater.* **25**, 6313–6333 (2013).
39. Y. Kang, M. K. Masud, Y. Guo, Y. Zhao, Z. S. Nishat, J. Zhao, B. Jiang, Y. Sugahara, T. Pejovic, T. Morgan, M. S. A. Hossain, H. Li, C. Salomon, T. Asahi, Y. Yamauchi, Au-loaded superparamagnetic mesoporous bimetallic CoFeB nanovehicles for sensitive autoantibody detection. *ACS Nano* **17**, 3346–3357 (2023).
40. S. Chu, A. Majumdar, Opportunities and challenges for a sustainable energy future. *Nature* **488**, 294–303 (2012).
41. Y. Kang, O. Cretu, J. Kikkawa, K. Kimoto, H. Nara, A. S. Nugraha, H. Kawamoto, M. Eguchi, T. Liao, Z. Sun, T. Asahi, Y. Yamauchi, Mesoporous multimetallic nanospheres with exposed highly entropic alloy sites. *Nat. Commun.* **14**, 4182 (2023).
42. Z.-Y. Yu, Y. Duan, X.-Y. Feng, X. Yu, M.-R. Gao, S.-H. Yu, Clean and affordable hydrogen fuel from alkaline water splitting: Past, recent progress, and future prospects. *Adv. Mater.* **33**, e2007100 (2021).
43. X.-L. Zhang, P.-C. Yu, X.-Z. Su, S.-J. Hu, L. Shi, Y.-H. Wang, P.-P. Yang, F.-Y. Gao, Z.-Z. Wu, L.-P. Chi, Y.-R. Zheng, M.-R. Gao, Efficient acidic hydrogen evolution in proton exchange membrane electrolyzers over a sulfur-doped marcasite-type electrocatalyst. *Sci. Adv.* **9**, eadh2885 (2023).
44. Y. Zhao, P. V. Kumar, X. Tan, X. Lu, X. Zhu, J. Jiang, J. Pan, S. Xi, H. Y. Yang, Z. Ma, T. Wan, D. Chu, W. Jiang, S. C. Smith, R. Amal, Z. Han, X. Lu, Modulating Pt-O-Pt atomic clusters with isolated cobalt atoms for enhanced hydrogen evolution catalysis. *Nat. Commun.* **13**, 2430 (2022).
45. Y. Shi, Z.-R. Ma, Y.-Y. Xiao, Y.-C. Yin, W.-M. Huang, Z.-C. Huang, Y.-Z. Zheng, F.-Y. Mu, R. Huang, G.-Y. Shi, Y.-Y. Sun, X.-H. Xia, W. Chen, Electronic metal–support interaction modulates single-atom platinum catalysis for hydrogen evolution reaction. *Nat. Commun.* **12**, 3021 (2021).
46. H. Gao, Y. Jiang, R. Chen, C.-L. Dong, Y.-C. Huang, M. Ma, Z. Shi, J. Liu, Z. Zhang, M. Qiu, T. Wu, J. Wang, Y. Jiang, J. Chen, X. An, Y. He, S. Wang, Alloyed Pt single-atom catalysts for durable PEM water electrolyzer. *Adv. Funct. Mater.* **33**, 2214795 (2023).
47. N. Cheng, S. Stambula, D. Wang, M. N. Banis, J. Liu, A. Riese, B. Xiao, R. Li, T.-K. Sham, L.-M. Liu, G. A. Botton, X. Sun, Platinum single-atom and cluster catalysis of the hydrogen evolution reaction. *Nat. Commun.* **7**, 13638 (2016).
48. J. Liu, J. Liao, K. Huang, J. Dong, G. He, Z. Gong, H. Fei, A general strategy to remove metal aggregates toward metal–nitrogen–carbon catalysts with exclusive atomic dispersion. *Adv. Mater.* **35**, 2211398 (2023).
49. X. Cheng, B. Xiao, Y. Chen, Y. Wang, L. Zheng, Y. Lu, H. Li, G. Chen, Ligand charge donation–acquisition balance: A unique strategy to boost single Pt atom catalyst mass activity toward the hydrogen evolution reaction. *ACS Catal.* **12**, 5970–5978 (2022).
50. S. Ye, F. Luo, Q. Zhang, P. Zhang, T. Xu, Q. Wang, D. He, L. Guo, Y. Zhang, C. He, X. Ouyang, M. Gu, J. Liu, X. Sun, Highly stable single Pt atomic sites anchored on aniline-stacked graphene for hydrogen evolution reaction. *Energ. Environ. Sci.* **12**, 1000–1007 (2019).
51. H. Wei, H. Wu, K. Huang, B. Ge, J. Ma, J. Lang, D. Zu, M. Lei, Y. Yao, W. Guo, H. Wu, Ultralow-temperature photochemical synthesis of atomically dispersed Pt catalysts for the hydrogen evolution reaction. *Chem. Sci.* **10**, 2830–2836 (2019).
52. X.-P. Yin, H.-J. Wang, S.-F. Tang, X.-L. Lu, M. Shu, R. Si, T.-B. Lu, Engineering the coordination environment of single-atom platinum anchored on graphdiyne for optimizing electrocatalytic hydrogen evolution. *Angew. Chem. Int. Ed.* **57**, 9382–9386 (2018).
53. J. Park, S. Lee, H.-E. Kim, A. Cho, S. Kim, Y. Ye, J. W. Han, H. Lee, J. H. Jang, J. Lee, Investigation of the support effect in atomically dispersed Pt on WO_{3-x} for utilization of Pt in the hydrogen evolution reaction. *Angew. Chem. Int. Ed.* **58**, 16038–16042 (2019).
54. H. Tian, X. Cui, L. Zeng, L. Su, Y. Song, J. Shi, Oxygen vacancy-assisted hydrogen evolution reaction of the Pt/WO_3 electrocatalyst. *J. Mater. Chem. A* **7**, 6285–6293 (2019).
55. K. Jiang, B. Liu, M. Luo, S. Ning, M. Peng, Y. Zhao, Y.-R. Lu, T.-S. Chan, F. M. F. de Groot, Y. Tan, Single platinum atoms embedded in nanoporous cobalt selenide as electrocatalyst for accelerating hydrogen evolution reaction. *Nat. Commun.* **10**, 1743 (2019).
56. Z.-W. Wei, H.-J. Wang, C. Zhang, K. Xu, X.-L. Lu, T.-B. Lu, Reversed charge transfer and enhanced hydrogen spillover in platinum nanoclusters anchored on titanium oxide with rich oxygen vacancies boost hydrogen evolution reaction. *Angew. Chem. Int. Ed.* **60**, 16622–16627 (2021).
57. D. Liu, X. Li, S. Chen, H. Yan, C. Wang, C. Wu, Y. A. Haleem, S. Duan, J. Lu, B. Ge, P. M. Ajayan, Y. Luo, J. Jiang, L. Song, Atomically dispersed platinum supported on curved carbon supports for efficient electrocatalytic hydrogen evolution. *Nat. Energy* **4**, 512–518 (2019).
58. J. Xu, C. Zhang, H. Liu, J. Sun, R. Xie, Y. Qiu, F. Lü, Y. Liu, L. Zhuo, X. Liu, J. Luo, Amorphous MoO_X-stabilized single platinum atoms with ultrahigh mass activity for acidic hydrogen evolution. *Nano Energy* **70**, 104529 (2020).
59. J. Ji, Y. Zhang, L. Tang, C. Liu, X. Gao, M. Sun, J. Zheng, M. Ling, C. Liang, Z. Lin, Platinum single-atom and cluster anchored on functionalized MWCNTs with ultrahigh mass efficiency for electrocatalytic hydrogen evolution. *Nano Energy* **63**, 103849 (2019).
60. J. Zhang, Y. Zhao, X. Guo, C. Chen, C.-L. Dong, R.-S. Liu, C.-P. Han, Y. Li, Y. Gogotsi, G. Wang, Single platinum atoms immobilized on an MXene as an efficient catalyst for the hydrogen evolution reaction. *Nat. Catal.* **1**, 985–992 (2018).
61. Y. Wu, W. Wei, R. Yu, L. Xia, X. Hong, J. Zhu, J. Li, L. Lv, W. Chen, Y. Zhao, L. Zhou, L. Mai, Anchoring sub-nanometer Pt clusters on crumpled paper-like MXene enables high hydrogen evolution mass activity. *Adv. Funct. Mater.* **32**, 2110910 (2022).
62. M. Sheng, Q. Wu, Y. Wang, F. Liao, Q. Zhou, J. Hou, W. Weng, Network-like porous Co-Ni-B grown on carbon cloth as efficient and stable catalytic electrodes for hydrogen evolution. *Electrochem. Commun.* **93**, 104–108 (2018).
63. T. Shinagawa, A. T. Garcia-Esparza, K. Takanabe, Insight on Tafel slopes from a microkinetic analysis of aqueous electrocatalysis for energy conversion. *Sci. Rep.* **5**, 13801 (2015).
64. Z. Xia, S. Guo, Strain engineering of metal-based nanomaterials for energy electrocatalysis. *Chem. Soc. Rev.* **48**, 3265–3278 (2019).
65. M. Du, D. Li, S. Liu, J. Yan, Transition metal phosphides: A wonder catalyst for electrocatalytic hydrogen production. *Chin. Chem. Lett.* **34**, 108156 (2023).
66. G. Kresse, D. Joubert, From ultrasoft pseudopotentials to the projector augmented-wave method. *Phys. Rev. B* **59**, 1758–1775 (1999).
67. J. P. Perdew, K. Burke, M. Ernzerhof, Generalized gradient approximation made simple. *Phys. Rev. Lett.* **77**, 3865–3868 (1996).
68. S. Grimme, J. Antony, S. Ehrlich, H. Krieg, A consistent and accurate ab initio parametrization of density functional dispersion correction (DFT-D) for the 94 elements H-Pu. *J. Chem. Phys.* **132**, 154104 (2010).
69. V. Wang, N. Xu, J.-C. Liu, G. Tang, W.-T. Geng, VASPKIT: A user-friendly interface facilitating high-throughput computing and analysis using VASP code. *Comput. Phys. Commun.* **267**, 108033 (2021).

Acknowledgment: Y.K. thanks the support from JSPS Postdoctoral Fellowships for Research in Japan. **Funding:** This work was supported by the JST-ERATO Yamauchi Materials Space-Tectonics Project (JPMJER2003). This work was also supported by the National Key Research and Development Program of China (SQ2020YFA020032), the National Natural Science Foundation of China (22236005, 22108238, and 22376142), and Shanghai Government

(22dz1205400, 23520711100, and 22010503400). **Author contributions:** Y.Y. and H.L. conceived and supervised the research. Y.K. and Y.Y. designed the experiments and wrote the paper. Y.K. performed most of the experiments and data analysis. O.C. and K.K. performed the TEM and EELS characterization and data analysis. S.L., X.W., and D.Z. processed and analyzed the XAF data. B.J. supported the theoretical calculations. Y.Z., L.Z., L.F., D.J., C.W., and T.A. participated in the experiments and discussions. All authors discussed the results and commented on the manuscript. **Competing interests:** The authors declare that they have no competing interests. **Data and materials availability:** All data needed to evaluate the conclusions in the paper are present in the paper and/or the Supplementary Materials.

Submitted 24 January 2024
Accepted 14 May 2024
Published 21 June 2024
10.1126/sciadv.ado2442